Recent results of the T-10 tokamak

V.A. Vershkov[1]**, V.F. Andreev**[1]**, A.A. Borschegovskiy**[1]**,**
V.V. Chistyakov[1]**, M.M. Dremin**[1]**, L.G. Eliseev**[1]**, E.P. Gorbunov**[1]**,**
S.A. Grashin[1]**, A.V. Khmara**[1]**, A.Ya. Kislov**[1]**, D.A. Kislov**[1]**,**
A.D. Komarov[2]**, A.S. Kozachek**[2]**, V.A. Krupin**[1]**, L.I. Krupnik**[2]**,**
S.V. Krylov[1]**, S.E. Lysenko**[1]**, S.G. Maltsev**[1]**, V.A. Mavrin**[1]**,**
A.V. Melnikov[1]**, G.E. Notkin**[1]**, A.Yu. Novikov**[1]**, Yu.D. Pavlov**[1]**,**
S.V. Perfilov[1]**, V.V. Piterskij**[1]**, G.N. Ploskirev**[1]**, V.I. Poznyak**[1]**,**
K.A. Razumova[1]**, I.N. Roy**[1]**, D.V. Ryzhakov**[1]**, P.V. Savrukhin**[1]**,**
E.A. Shestakov[1]**, D.A. Shelukhin**[1]**, Yu.A. Skosyrev**[1]**,**
R.V. Shurygin[1]**, G.N. Tilinin**[1]**, E.V. Trukhina**[1] **and V.M. Trukhin**[1]

[1] NRC 'Kurchatov Institute', 123182 Moscow, Russia
[2] Institute of Plasma Physics, NSC KIPT, 310108 Kharkov, Ukraine

E-mail: vershkov@nfi.kiae.ru

Abstract

Poloidal asymmetry and radial correlation lengths of turbulence were investigated in T-10 at low field side and high field side by correlation reflectometry. Correlation of plasma confinement with the turbulence type was observed. Improvements in heavy ion beam probe diagnostic enabled us to measure the plasma potential during electron cyclotron resonance heating (ECRH) in a wide range of radial positions and operational regimes. The turbulence appeared to rotate close to $E \times B$ velocity. The concept of electron internal transport barrier (e-ITB) formation at low-order rational surfaces under conditions of low density of the rational surfaces was proved by the observation of e-ITB formation near the $q = 1.5$ surface in discharges with non-central ECRH and current ramp-up. The kinetic phenomena were investigated by means of electron cyclotron emission (ECE) under the strong on-axis ECRH. Lithium gettering of the limiter and the wall allowed us to significantly reduce the impurity level and obtain a recycling coefficient as low as 0.3. The rates of carbon film deposition were measured in the working and cleaning discharges. Second harmonic EC assisted start-up was investigated. ECRH allowed us to control the generation of runaway electrons and the current decay rate after the energy quench at the density limit disruption.

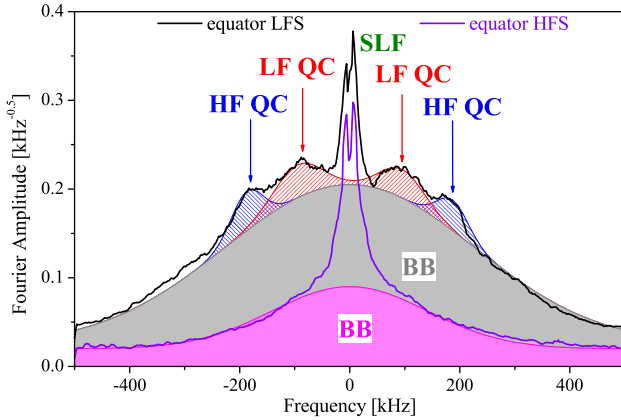(Some figures in this article are in colour only in the electronic version)

1. Introduction

T-10 is a medium-sized circular tokamak with major and minor radii $R = 1.5$ and $a = 0.3$ m, respectively. The maximal toroidal magnetic field is $B_T = 2.5$ T and the plasma current is up to $I_p = 350$ kA. T-10 has an auxiliary second harmonic electron cyclotron resonance heating (ECRH) gyrotron system with power up to 2 MW with two frequencies: 140 and 130 GHz, which enables us to vary the input heating power profile. Lithium gettering allows us to work with a reduced recycling coefficient (as low as 0.3) and to clean the plasma. T-10 experiments were carried out in ohmic and ECRH discharges. The main topics of investigations were the physics of core anomalous transport of different plasma species, the core and scrape-off layer (SOL) variations under lithium gettering and second harmonic EC-assisted start-up of discharge. The characteristic features of the core investigations were the wide variation of the ECRH radial power profile, the
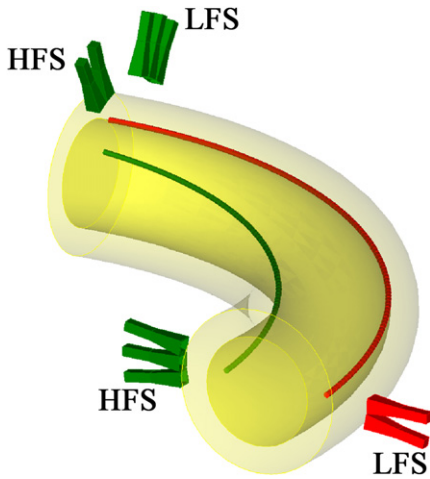
full coverage of the radial and poloidal turbulence distributions with correlation reflectometry (CR) and the measurements of the plasma potential by heavy ion beam probing (HIBP).

2. Spatial structure of small-scale density fluctuations studied by correlation reflectometry

Identification of the physical mechanisms of small-scale turbulence is important for investigations of anomalous plasma transport. A review of the experimentally observed types of turbulence at the low field side (LFS) in T-10 can be found in [1]. The first results of turbulence investigation at the high field side (HFS) revealed a strong poloidal asymmetry of turbulence [2]. The typical amplitude Fourier spectra of turbulence, measured at LFS and HFS are shown in figure 1. The characteristic features of the LFS spectra are the presence of maxima near 70, 150 kHz and zero frequencies, and the
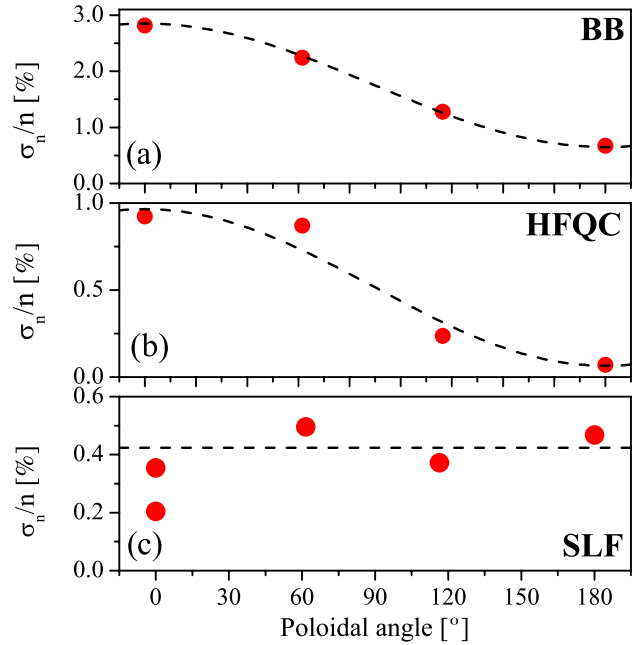
Figure 1. Fourier spectra of reflectometer signals at LFS (black) and HFS (purple).

Figure 2. Schematics of the reflectometry antenna array positions on T-10.

Figure 3. Poloidal dependence of relative level of density perturbation σ_n/n for different fluctuations types.

significantly higher level with respect to HFS. These maxima were referred to as low-frequency and high-frequency quasi-coherent oscillations (LF QC and HF QC, respectively) and stochastic low-frequency (SLF) fluctuations. It was shown [1] that the characteristics of LF QC are similar to the theoretically predicted ion temperature gradient (ITG) instability, and HF QC to the trapped electron mode (TEM). The modes were identified in [1] in accordance with their values of $k_\perp \rho_\mathrm{i}$ ($k_\perp$ is the wave number and ρ_i is the Larmor radius), their dependences on the discharge parameters and radial profiles of amplitude. All of these maxima are superimposed on the broadband (BB) turbulence background.

The spatial structure of turbulence was studied in detail by correlation reflectometry [1]. For this purpose, a new antenna array was installed at LFS. The final scheme of the antenna arrays is shown in figure 2 (new antenna is marked by red). It includes antenna arrays at poloidal angles about $+60°$ and $+120°$ in the poloidal cross section A, and antenna arrays at poloidal angles about $0°$ and $+180°$ in the poloidal cross section D. Zero poloidal angle corresponds to the equatorial plane at LFS. The toroidal angle between poloidal cross sections A and D is equal to $90°$. The new antenna system allows us to measure (1) the whole poloidal turbulence asymmetry from four poloidal angles; (2) radial correlations at LFS and HFS; (3) lo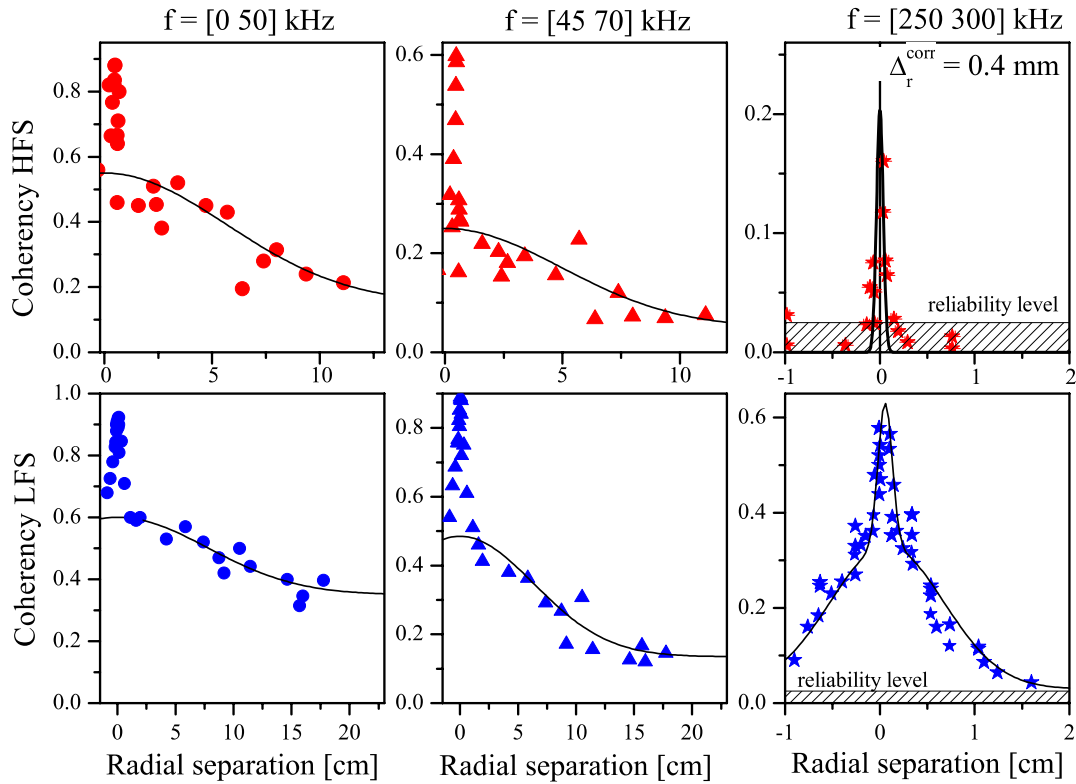ng-distance toroidal correlations along the magnetic field line at LFS and HFS (as shown in figure 2 by helical lines); (4) turbulence variation at HFS/LFS with density and current. Although all of these measurements are in progress, this paper deals only with the first two topics, because the latter two need additional work and will be published elsewhere.

The poloidal variations of the different turbulence types are presented in figure 3. The experiments were carried out in an ohmic discharge with $I_\mathrm{p} = 250\,\mathrm{kA}$, $B_\mathrm{T} = 2.4\,\mathrm{T}$ and $n_\mathrm{e} = 2.7 \times 10^{19}\,\mathrm{m}^{-3}$ at a radius of about $2/3a$. A strong asymmetry of the random-mean-square value (RMS, σ_n) of the amplitude of small-scale density perturbation was found at different poloidal angles. This asymmetry could be characterized by the ratio of the RMS values of perturbation at LFS and HFS. The highest asymmetry is observed for HF QC, figure 3(*b*), and it is equal to about 13. BB turbulence has an asymmetry of about 4, figure 3(*a*), while SLF fluctuations, figure 3(*c*), are independent of the poloidal angle. Hence, we can conclude that the quasi-coherent oscillations are the feature of the LFS, as predicted by the 3D gyrokinetic codes for the drift waves [3]. However, the high asymmetry of the HF QC raises the question about lower asymmetry of the BB, because earlier [1] both phenomena were described by the same physical mechanism. First we should investigate the difference in the properties of the BB at LFS and HFS, and then the radial localization of SLF feature. Due to the rather long radial and poloidal correlation lengths of SLF [1], strong non-local effects are expected, when ordinary wave (O-mode) reflectometry is used to measure the turbulence characteristics in the plasma core. This effect becomes stronger due to the high turbulence level at the plasma edge.

2.1. Radial correlation measurements

Detailed radial correlation measurements were carried out in similar discharges at LFS and HFS, using the correlation
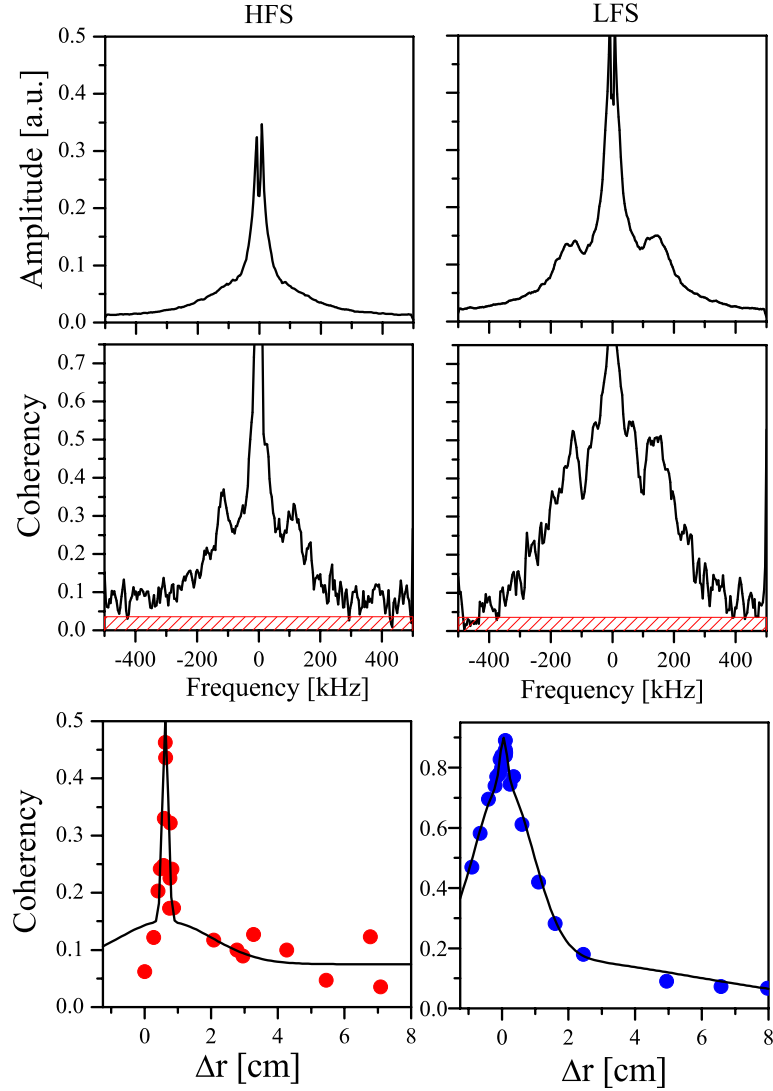
Figure 4. Radial cross-correlation functions for different frequency bands at HFS (top) and LFS (bottom).

between O-mode signals, and between signals in O-mode and low-frequency cut-off of extraordinary wave (XL mode). In addition, BB and SLF features were explored in experiments with amplitude modulation (AM) reflectometry and with long-distance toroidal correlations. New measurements of radial correlations with two O-mode reflectometers for HFS and LFS are presented in figure 4 (top and bottom panels, respectively). The experiments were carried out in similar regimes with $B_T = 2.4$ T, $I_p = 250$ kA and $n_e = 1.6 \times 10^{19}$ m^{-3}. Two heterodyne reflectometers were used with frequency ranges from 36 to 55 GHz and from 25.5 to 37 GHz, i.e. they overlap in the range from 36 to 37 GHz. The experiment showed that the minimal possible frequency difference was 80 MHz due to the significant cross-talk between two reflectometers, resulting in unstable work. The frequencies were constant during the discharge and changed from shot to shot. Figure 4 (top panel) shows the coherency dependence on the distance between reflecting layers for the low-frequency band at HFS. After a sharp initial decrease, attributed to BB, we see a slow decrease with $\lambda_r = 7.5$ cm and some residual background, which is typical for SLF. Further evolution of the correlation function with an increase in the frequency band is also shown in figure 4. The SLF feature in the radial correlation function relatively decreases with the increase in the analysed spectral frequency band. SLF traces disappear at frequencies higher than 100 kHz. Also a very narrow peak with $\lambda_r = 0.4$ mm exists in all frequency bands, and it becomes the only one at the high-frequency band (right panels).

The long correlation length for SLF just confirms our previous results [1]. However, the new experimental correlation length for HFS BB was an order of magnitude less

than that at LFS. This raised the question about the radial resolution of reflectometry. Such a correlation length was about 1/20 from the probing reflectometry wavelength. 2D full-wave simulation of the electromagnetic wave reflection from the turbulent plasma was performed for the realistic T-10 geometry. The model of turbulence includes random Gaussian perturbations with widths of 3.5, 2.5 and 1 mm. Simulations demonstrate that the radial correlation length is independent of perturbation size, and reflected signals have the same correlation lengths about 7 mm. These results are consistent with theoretical predictions [4].

This question stimulated new experiments at LFS under exactly the same conditions. The LFS antenna array in sector A at 60° to the equatorial plane was used to reproduce our previous results and for technical reasons (see figure 2). The results for the LFS are presented in figure 4 (bottom panels) from low to higher fluctuation frequency bands, respectively. Qualitatively the results at LFS are similar to the HFS. There are two main features: SLF turbulence with long correlation lengths, which dominates at low-frequency bands, and BB fluctuations with short correlation length that dominate at higher frequencies. Nevertheless, there are significant differences in LFS correlations with respect to HFS ones. First, the SLF turbulence has very long correlation lengths. At low frequencies, SLF correlated practically over the whole column, which may suggest the lack of locality of reflectometry for long wavelength turbulence. Second, in all frequency bands, BBs at LFS have two distinct components (see figure 4 bottom, right): a very narrow peak with $\lambda_r = 1$ mm on the top of a wider correlation function with $\lambda_r = 3.5$ mm. The former appears like the HFS BB and gives about 40%

Figure 5. Fourier spectra of signal (top) and radial coherency (middle) for HFS (left) and LFS (right). Red shaded regions on the middle plots show confidence level. Radial coherency function determined for frequencies 90–150 kHz (bottom).

contribution to the total correlation value. The latter is the special feature of the LFS and its contribution is about 60%. Taking into account the BB asymmetry 2.5 (see figure 3 for the poloidal angle 60°), we may formally suggest that there are two different turbulence components: the poloidally symmetrical short correlated component with $\lambda_r = 1$ mm (40% at LFS) and turbulence, specific only for the LFS, with $\lambda_r = 3.5$ mm (60% at LFS). This accounts for the integral BB asymmetry of 2.5. However, in any case such formal decomposition cannot explain the observed extremely short correlation lengths. It was already mentioned that 2D simulation with Gaussian perturbations cannot explain λ_r shorter than 7 mm. But, in accordance with theory, it is possible to expect shorter λ_r with oscillatory perturbations [4]. In fact, for the HFS, such perturbations are predicted by 3D gyrokinetic simulations [3] due to the toroidal coupling of the perturbations at the high-order rational surfaces under conditions of non-zero magnetic shear [1]. Under such conditions, the radially elongated structures at the equatorial LFS (which was associated in [1] with quasi-coherent turbulence) transformed to the two
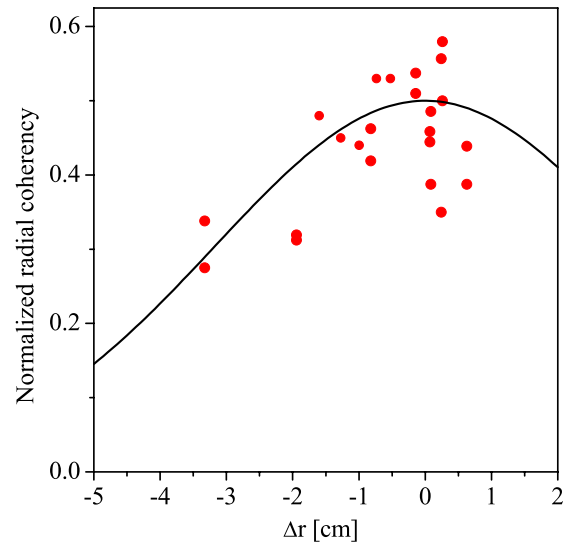
sets of highly spiral structures at HFS. Superposition of such structures could lead to the formation of oscillatory perturbations with typical radial size about $\lambda_r \cong 1$ mm. This hypothesis is confirmed by the experiments with long-distance toroidal correlations at the HFS [2]. It was shown that the correlation length of the QC turbulence is larger than one turn around the major tokamak axis. Under the given experimental conditions, the value $q < 2$ means that the HFS/LFS connection length L is less than $2\pi R$.

The presence of the maxima of the LF QC at a frequency of about 120 kHz in coherency spectra is clearly seen at LFS and HFS in figure 5. While the coherency spectra look similar, the amplitude spectra are different. And the radial correlation lengths for the frequency band around 120 kHz (shown in figure 4, bottom panels) differ by an order of magnitude. These facts are in good agreement with the hypothesis on the toroidal modes coupling. The natural question, of what the mechanisms of transformation of rather defined QC frequency into the wide frequency range of BB are, should be considered. The case is that at the LFS, the QC structures are radially

elongated, and their frequencies are determined by the Doppler mechanism due to the plasma rotation. In contrast, at HFS there are complex structures with two sets of spiral QC. Hence, the structures become significantly stretched poloidally and form radially oscillating perturbations with two signs of helicity. In addition, experiments with long-distance toroidal correlations at the HFS [2] and new experiments at LFS have shown that QC fluctuations travel as drift turbulence at angles inside $\pm 0.5°$ to the magnetic field line. This fact will result in an additional stochastization of QC at HFS after travelling a distance of about 10 m from LFS to HFS. It is natural to consider the application of the same mechanism for the formation of BB at LFS. In these terms, the 40% shortly correlated part corresponds to the QC coming toroidally from long distances, compared with one toroidal turn, while the 60% with $\lambda_r = 3.5$ mm arises from the fluctuations originated from the regions near LFS. Due to the lower connection length they have less helicity and higher λ_r. Finally, the QC fluctuations, originated near the observation region, will be seen like QC with a definite maximum in the turbulence spectrum. The considered hypothesis did not exclude the co-existence of the two different turbulence types: poloidally symmetrical with a short correlation length ($\lambda_r \cong 1$ mm) and specific only for the LFS fluctuations with $\lambda_r \cong 3.5$ mm.

2.2. Characteristics of SLF turbulence

The SLF turbulence covers the frequency band from several to 100 kHz. The main property of SLF is the poloidal uniformity and radial correlation length of about 6–10 cm (see figure 4(*d*)). The characteristic poloidal size of SLF fluctuations was about 5 cm. Hence, such long-wave fluctuations may be treated in 1D approximation. It is well known that the relative density fluctuations at the plasma edge in OH and L-modes may reach 10–50%, and their spectral maximum is just in the low-frequency band [1]. Thus, the case where most of SLF turbulence originated from the edge should be considered. In order to estimate the edge turbulence effect on the radial correlation measurements, 1D model simulations were performed. The strong edge turbulence ($dn/n = 10\%$) at the limiter was superimposed with the core ($dn/n = 0.5\%$). The modelling was performed for radial correlations of two O-modes, O-mode with XL mode, correlations of two XL modes and the correlations of two amplitude modulated (AM) XL modes. It was found that the correlation of the two O-modes is the worst case, the correlation of the O and XL modes is much better. Note that the low sensitivity of the XL mode to edge fluctuations is the specific feature of this mode. The correlations of the two XL mode signals make the situation much better, and the correlation of the two AM modulated XL mode signals could give the best estimation of radial size of perturbations. Hence, according to the simulations, a significant improvement of SLF radial localization may be obtained by the correlations of O and XL modes, which was carried out experimentally at the HFS. The discharge parameters were close to the discharge with the radial O-mode correlations, except the higher density $n_e = 2.5 \times 10^{19}$ m^{-3}. Reflectometry with O-mode had the frequency range from 36 to 55 GHz, and for XL mode—from 25.5 to 37 GHz, respectively. Typical position of the reflection layer was at the minor radius $r = 20$ cm for both O- and XL-mode reflections.

Figure 6. Correlation at HFS of O-mode at 51 GHz and XL mode (around 25.5 GHz) in a frequency band 20–50 kHz.
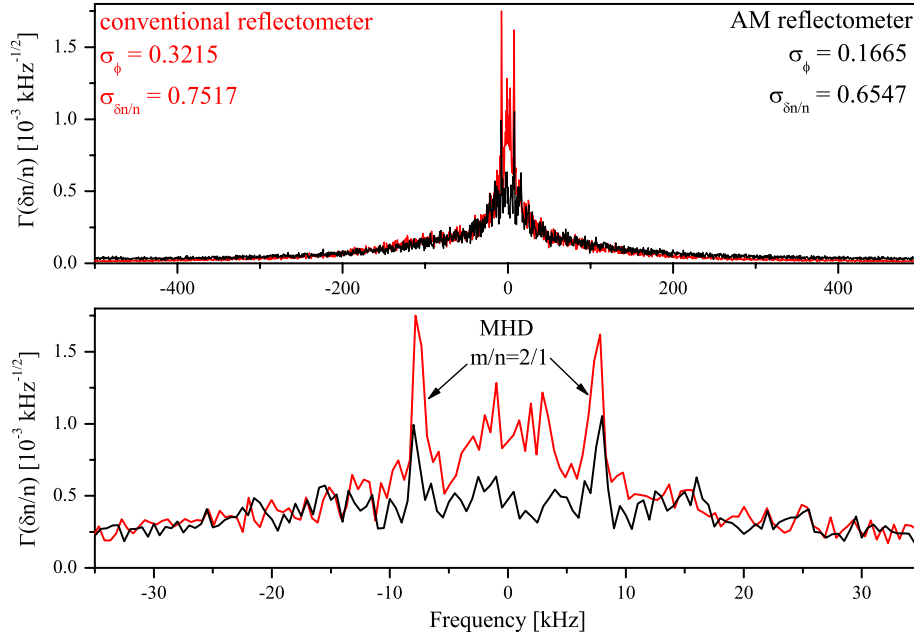
The result of such an experiment at HFS is presented in figure 6. In accordance with the simulations, the localization of SLF turbulence became better, and measurements gave the radial correlation length for SLF fluctuations to be about $\lambda_r = 4.5$ cm. Further improvement of the SLF localization may be achieved by the application of amplitude modulation of XL mode with a frequency $F_{mod} = 80$ MHz. Conventional reflectometry measures the fluctuations of the phase of the main launched wave. In contrast, AM reflectometry measures the phase fluctuations of the wave envelopes. The resulting spectra for the conventional XL HFS reflectometry and the AM XL one are compared in figure 7. This improvement enables us to prove the existence of SLF at the HFS in the core region with radii less than 2/3a.

Additional evidence of the core SLF was obtained during the long-distance toroidal correlation experiments at HFS and LFS. SLF fluctuations were found at the HFS with $r = 16$ cm [2], while SLF was not detected at the LFS at $r = 21.5$ cm. Hence, these results additionally proved the core SLF location with radii less than 2/3a (20 cm). The correlation reflectometry measurements with the XL mode were performed in the FTU tokamak with similar dimensions, where the SLF turbulence was clearly seen [5]. Hence, we can conclude that SLF turbulence is present in the core regions of tokamaks at the HFS and LFS. The SLF turbulence has a constant phase along the magnetic field line [2] that is typical both for the magnetic and interchange turbulence.

3. Correlation of plasma transport with type of turbulence

The transport of different plasma species, including impurities, the ion and electron heat transport, and their correlation with turbulence characteristics were studied in various ohmic discharges [6]. Experiments were carried out in a wide range of plasma densities, $0.4 < n_e < 5.6 \times 10^{19}$ m^{-3}.

Diffusion of He ions and the ion temperature profiles were measured with the recently developed charge

Figure 7. Fourier spectra of conventional (red) and AM (black) reflectometers at HFS. Bottom plot—zoomed low-frequency region of spectra.

exchange recombination spectroscopy (CXRS) diagnostic, which uses a diagnostic hydrogen neutral beam. At low densities, low-frequency quasi-coherent (ITG) modes dominate. Intermediate densities are characterized by high-frequency quasi-coherent (TEM) modes. The instability type was identified in accordance with [1] and briefly described in section 2.
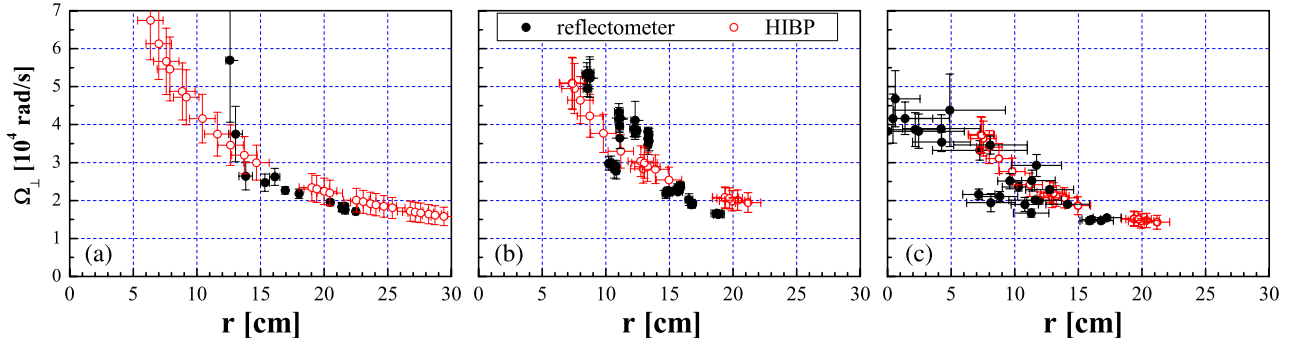
Argon and He confinement times (τ_{Ar}, τ_{He}) were obtained from the time evolution of their concentrations at the plasma centre after a short gas puff. As both gases have recycling near 100%, after puff their concentrations approached a stationary level. The characteristic times of this process were taken as the confinement times (τ_{Ar}, τ_{He}). The evolution of the central argon concentration was estimated from the emission of the Ar^{16+} line, and from the He^{2+} line obtained by CXRS. The argon confinement times τ_{Ar} were obtained in steady-state discharges after a short gas puff. Confinement of He and Ar impurities was similar. The measured τ_{Ar} was independent of density in a wide range of intermediate densities, and strongly decreased at low densities, where the ITG turbulence became dominant. Also good agreement of the central ion temperature value with the neoclassical 'Artsimovich expression' [7] was found at intermediate densities, while significantly lower temperatures were measured with a decrease in density [6]. At high densities the increase in the gas influx resulted in a degradation of confinement and decrease in the ion temperature. The degradation of confinement was also accompanied by a turbulence transition from TEM to ITG mode. When the gas influx decreases, the confinement, the ion and the electron temperatures increase, while the turbulence transits back from ITG to TEM. Hence, experiments show good correspondence of the ion confinement degradation with the developments of ITG instability at low densities, and high influx in discharges with high densities.

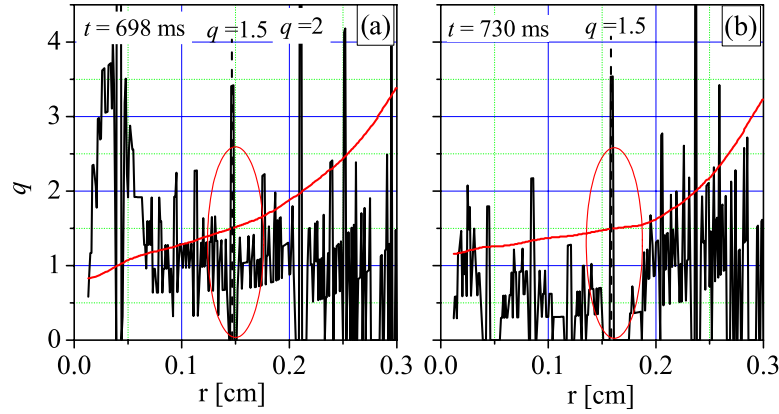**Table 1.** Parameters of discharges studied by HIBP and CR.

Regime	$\overline{n}_e$ (10^{19} m^{-3})	E_r (V cm^{-1})	Δr (cm)	B_T (T)	I_p (kA)	τ_E (ms)
I	1.3	55	6–30	1.55	140	20
II	2.4	65	6–30	1.55	140	36
III	2.5	70	7–22	2.08	165	38
IV	4.1	90	16–27	2.4	210	50

4. Measurements of plasma potential, radial electric field and turbulence rotation velocity

The absolute value of the core plasma potential φ and its fluctuations were measured by HIBP [8, 9]. The Tl$^+$ beam energy of HIBP was increased up to $E_b = 300$ keV, and the beam current up to $200\,\mu$A. This allows us to observe the core potential at high densities and in a wide radial area for the first time. The regimes with ohmic, on- and off-axis ECR heating ($B_T = 1.55$–2.4 T, $I_p = 140$–250 kA, $\overline{n}_e = (1.3$–4.1$) \times 10^{19}$ m^{-3}, $P_{EC} < 1.5$ MW) were studied, see table 1. The $\varphi(r)$ profile presents a linear function, and the slope of the profile allows us to estimate the mean radial electric field E_r. The potential well becomes deeper, and E_r becomes more negative with the increase in density and the energy confinement time τ_E. This result is consistent with earlier measurements in TM-4 [10] and TJ-II [11]. No strong irregularity is observed in the $\varphi(r)$ profile in the area of ECRH power deposition. The broadband turbulence rotation velocity Ω_{TURB} was measured by CR in regimes I and III together with $E \times B$ plasma rotation $\Omega_{E \times B}$ measured by HIBP. Figure 8 shows that $\Omega_{TURB}(r)$ is close to $\Omega_{E \times B}(r)$ in the whole observed ranges of radii, densities and toroidal magnetic fields both in OH and ECRH plasmas. Hence, we can conclude that within the experimental accuracy the turbulence does not have any additional intrinsic rotation in the $E \times B$ rotating frame.

Figure 8. Comparison of rotation velocities of density perturbations Ω_{TURB} from CR, with core plasma rotation $\Omega_{E \times B}$ from HIBP in OH ((*a*) $B_T = 1.55$ T; (*b*) $B_T = 2.08$ T) and ECRH (*c*) plasmas.

Figure 9. ASTRA calculation of $q(r)$ profile and the density of rational surface at ohmic stage (*a*) and after off-axis ECRH and current rump-up (*b*). Ellipses show regions of rarification of magnetic surfaces.

5. Role of rational surface density and self-organized pressure profile

In some theoretical papers [12–16] it was argued that the main plasma instabilities develop in the vicinity of rational surfaces and form turbulent cells. Cells with various poloidal and toroidal numbers m, n may overlap, and this may be the reason for the high anomalous thermal transport. It is clear that their possible maximal values M and N are limited for several reasons: too long magnetic lines may be destroyed by diffusion processes, the M value may be linked to several cells, whose dimensions are of the order of the ion Larmor radius, so at a given radius the possible number of cell in the poloidal direction has to be limited.

It has been noted in [12] that in the vicinity of low-order rational surfaces the gaps are located, where modes with m/n do not exist. In such gaps the turbulent cells are physically separated, and we have a low transport level as a result of location of such cells. We define the density of magnetic surfaces at minor radius r as the ratio of number of rational magnetic surfaces inside radial interval $[r - \rho_i; r + \rho_i]$ to the ion Larmor radius ρ_i.
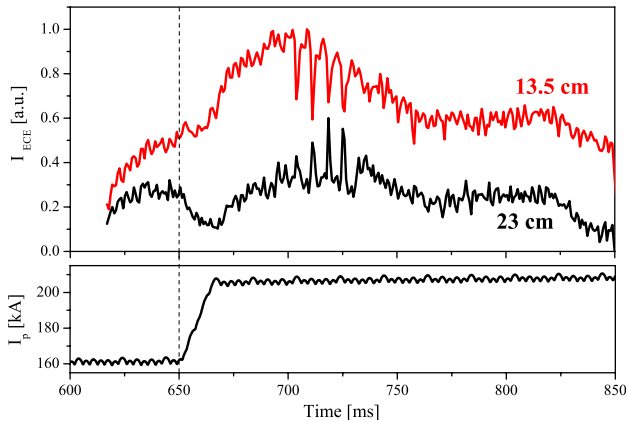
Previously it was demonstrated that ITBs are formed in the regions with very low or zero density of rational surfaces [17, 18]. Special experiments were carried out to check the role of rational surface density during the e-ITB formation. The main goal of these experiments was to dramatically change the density of the rational surfaces. Off-axis ECRH was used to suppress sawteeth oscillations, and then the plasma current was rapidly ramped with a rate up to 3 MA s^{-1} for 15 ms from $I_1 = 160$ kA to $I_2 = 206$ kA. The suppression of sawteeth oscillation and current ramp-up produce more flat q profile in the vicinity of rational surface $q = 1.5$ and form the region with low density of rational surfaces as one can see in figures 9(*a*) and (*b*).

The density profile was measured by a 12-chord radio-interferometer. This is not enough for good $n_e(r)$ reconstruction, but from previous experiments [16] we know that due to pump-out, n_e decreases in the power deposition region (14–15 cm) and increases inside and outside it. Hence, including $n_e(r)$ changes we can expect that the pressure gradient in ITB has to be steeper than the temperature one. Thus, the electron ITB appears in the vicinity of rational surface $q = 1.5$ after the start of off-axis ECRH, and the ITB improves after the current ramp-up. The time evolution of temperature inside ($r = 13.5$ cm) and outside ($r = 23$ cm) the e-ITB region is shown in figure 10.

The analysis of experiments showed that the conservation of self-consistence pressure profile $p_N(r)$ occurred in the regions where the turbulent cells overlapped and can be violated in the opposite case. Low electron heat conductivity in the ITB zone created by the off-axis ECRH was additionally analysed by means of heat pulse propagation (HPP) [19]. A slow HPP propagation, corresponding to $\chi_e^{HP} = 0.08$ m^2 s^{-1} was observed.

Figure 10. Time evolution of the temperature inside ($r = 13.5$ cm) and outside ($r = 23$ cm) the e-ITB region (off-axis ECRH starts at $t = 650$ ms). The temperature gradient is raised after ECRH start and increases after the current ramp-up.

6. Investigation of kinetic effects in plasma by means of ECE

The main method for plasma kinetics investigation at T-10 is the set of electron cyclotron resonance emission (ECE) diagnostics. Diagnostic could detect ECE signals in a wide frequency band in both X- and O-mode polarizations. It enables the measurements of both emissions of the thermal electrons of the relativistic electrons with energies up to 250–300 keV that give frequency downshifted ECE. The diagnostic set consists of two systems. The first includes multichannel receivers with 24 channels with a time resolution of about 1 µs. The removable frequency convertors permit us to measure an emission in first (38–78 GHz) or second (78–166 GHz) ECE harmonics. The second fast frequency scanning system (four receivers) is also applied for the investigation of ECE spectra including thermal and superthermal parts simultaneously in two polarizations: ordinary on first resonance (37–78 GHz) and extraordinary on second resonance (78–178 GHz). The time resolution for the full spectra is 0.5–1 ms. Measurements of ECE signals in both X- and O-mode polarizations enable us to evaluate the total, perpendicular and longitudinal energy of the radiant electrons. Emission of the extraordinary wave is determined only by the perpendicular electron energy while emission of the ordinary wave depends also on the longitudinal energy. According to the linear theory both polarizations are identical for the measurement of the electron temperature if the optical depth is sufficiently high. Different dynamics of signals points out directly to the non-Maxwellian electron distribution. Diagnostic complex includes also measurements of high-frequency (HF) plasma noises in the range of magnetized Langmuir oscillations (0.5–24 GHz). They are measured by small loop antennae insulated from a direct contact with the plasma.

Off-axis ECRH is applied to reveal the properties of $m/n = 1/1$ mode oscillations. Figure 11 shows the ECE signals in both polarizations from the same plasma volume of the central plasma zone ($r = 6$ cm) under low power heating (one off-axis gyrotron). Here the optical depth is about 4–5 and the measuring ECE is emitted by the main body of electron distribution. The dynamics of ECE amplitudes is similar (figure 11, left) but oscillations of X-ECE in $m/n = 1/1$ mode

are shifted in ~40–45 µs with respect to O-ECE (figure 11, right). This fact indicates that the anisotropy of electron distribution changes in every period of oscillations.
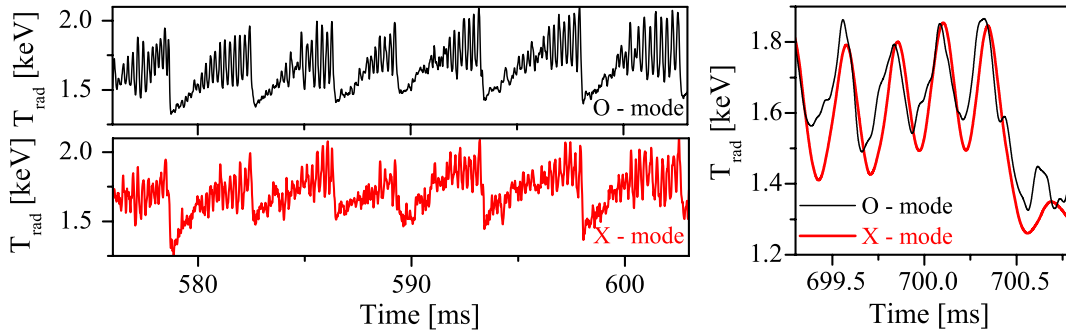
High-power ECRH (two off-axis and one on-axis gyrotrons) leads to stronger global oscillations and behaviour of O-mode ECE and X-mode ECE becomes different (figure 12). Significant difference occurs in the first stage of ECRH (figures 12-I(a)–(c)). Background of O-mode ECE exceeds that of X-mode ECE just after ECRH start. This fact points to the stretching of the distribution function in the longitudinal direction. Dashed lines for both ECE signals correspond to the X-mode ECE level just after internal disruptions. One could see that the deviation of electron distribution from thermodynamic equilibrium is minimal in those moments.

A considerably different dynamics of signals remains during the ECRH phase of discharge (figures 12-II(a)–(c)). Rise of the first harmonic O-mode ECE after disruption is several times higher than that for second harmonic X-mode. The amplitude of O-mode ECE slowly decreases during sawtooth oscillation and becomes minimal before the disruption. This behaviour could be explained by the distribution function's periodic deformation with two time scales: in every period of $m/n = 1/1$ oscillations (here $f \sim 3.5$ kHz) and during overall sawtooth cycles. Estimations show that the longitudinal velocity oscillates stronger than the perpendicular one though the second harmonic ECRH increases the transverse velocity of the electrons.
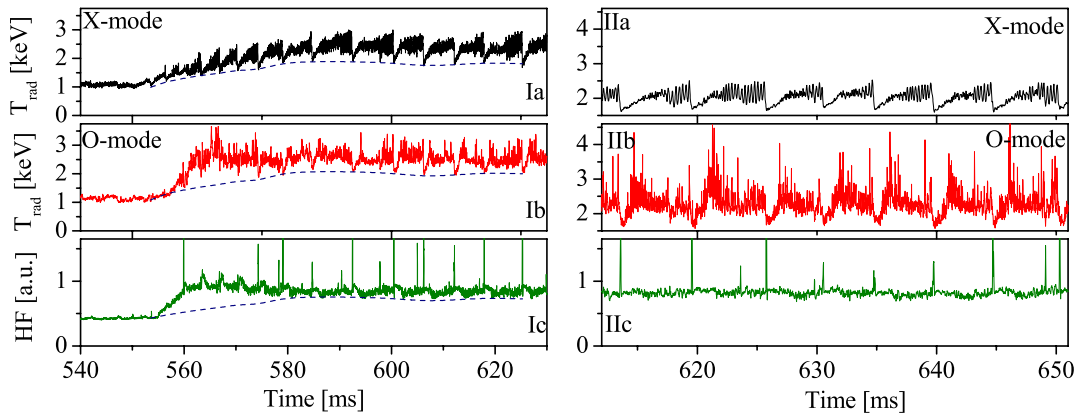
The background level of high-frequency plasma noises (HF) rises quickly with the start of ECRH and finally exceeds the OH level by a factor of two. Strong simultaneous spikes (in the low-frequency range of HF spectrum) at every internal disruption can surpass a background by more than one order of magnitude.

The intensive oscillations of the first harmonic O-mode ECE appear at the first stage of the on-axis ECRH at low frequencies (40–50 GHz), whereas ECR frequencies for typical T-10 discharges are 60–90 GHz. The frequencies of these ECE correspond to the emission outside the limiter radius of the plasma and could arise as frequency downshifted ECE created at the edge by the high-energy component of electrons. Figure 13 illustrates the O-mode ECE oscillations measured at different frequencies. The spikes at 50 GHz appeared just after the first internal disruption already in the OH phase. The emission frequency, where those ECE spikes are observed, decreases during ECRH. This means that the energy of electrons increases according to the relativistic effect up to some maximal value (here 190–220 keV). A similar emission was also observed for X-mode ECE but its amplitudes are smaller by more than one order of amplitude. This means that those spikes could be caused by high-energy electrons with mainly longitudinal energy.
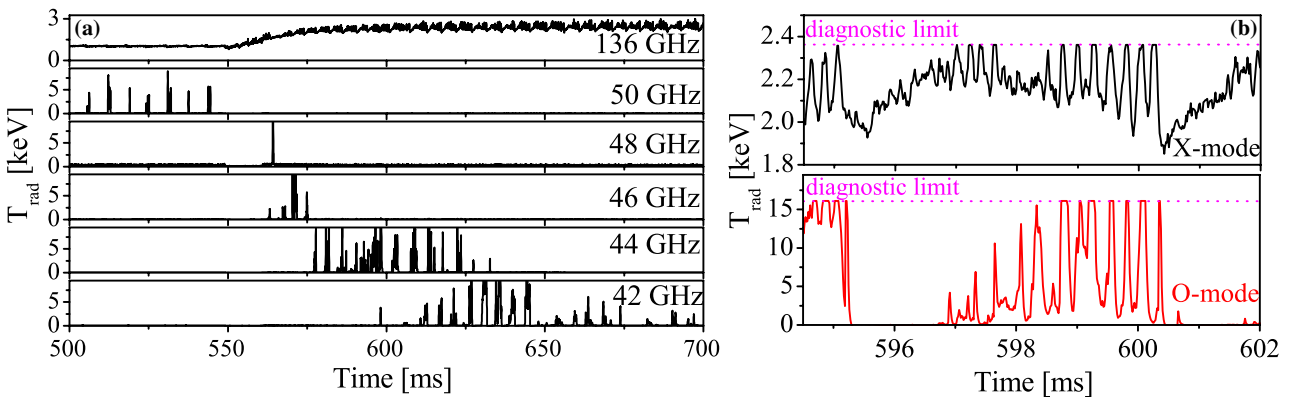
Bursts of the periphery ECE occur synchronously with the oscillations in $m/n = 1/1$ mode at the plasma centre. Edge localization of downshifted ECE emission was proved by means of edge density variation. The observation of the edge downshifted ECE emission becomes impossible when the O-mode cut-off layer is in the SOL region. The bursts of the high-energy electrons suppose presence of the strong pulsing longitudinal electric field up to ~0.1–1 V cm^{-1} in

Figure 11. Radiative temperature calculated from EC emission measurements during low power ECRH (one off-axis gyrotron): left top panel—second harmonic X-mode; left bottom panel—first harmonic O-mode; right panel—phase difference between ECE signals on the first harmonic O-mode and the second harmonic X-mode.

Figure 12. Time traces of radiative temperature calculated from EC emission measurements on the second harmonic X-mode (*a*), the first harmonic O-mode (*b*), and the HF plasma noise signal in frequency band 1–16 GHz (*c*). Left panels (I)—first stage of ECRH, dashed lines are the minimal level of X-mode ECE background; right panels (II)—steady-state of ECRH, specific difference in behaviour of O- and X-mode ECE signals continues up to the end of ECRH. Measurements were made under strong ECRH with a total power of about 1.5 MW (two off-axis and one on-axis gyrotrons).
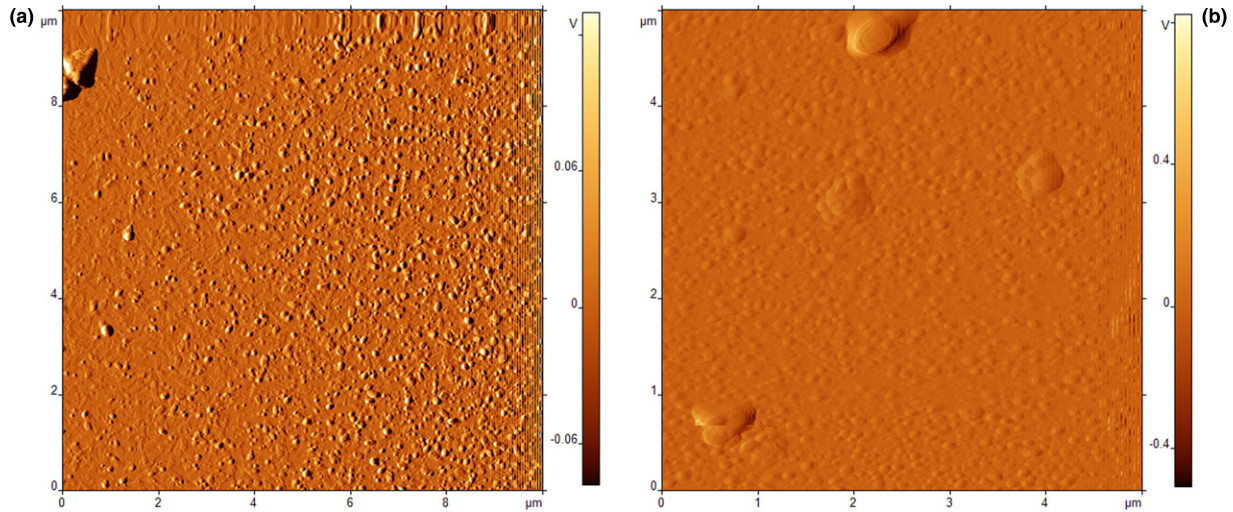

Figure 13. Time traces of ECE in the second harmonic X-mode from the plasma centre and the first harmonic O-mode from the plasma edge: (*a*) OH stage and first stage of ECRH and (*b*) one period of sawtooth.

plasma. Such fields may be produced by the plasma current relaxation in the central plasma area (mode $m/n = 1/1$). The synchronous behaviour of the oscillations at the plasma core and boundary shows apparently a strong coupling of the core and edge of the plasma.

7. Experiments with lithium gettering

Lithium gettering of the limiter and the wall allows us to reduce significantly the impurity level and obtain the recycling

coefficient less than 0.3. The first results of the experiments with Li gettering were presented at the 2008 IAEA Conference [20]. The recent results concerned with the detailed analysis of the Li distribution over the rail limiter and the estimation of absolute Li outflux by Li pellet injection. One of the characteristic features of the Li behaviour in T-10 is a very slow Li migration along the tokamak chamber. There were four T-10 campaigns with 14 Li gettering. The estimated total amount of Li introduced into the chamber was about 20 g. However, neither the spectroscopy nor the chamber inspection
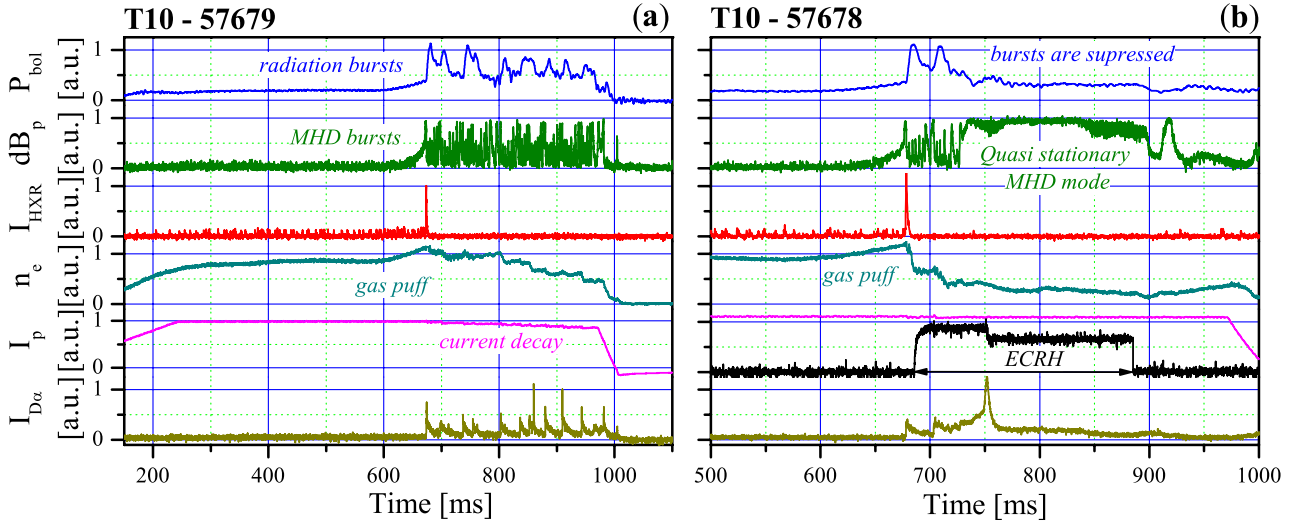
Figure 14. (*a*) Globular structure of the film, deposited in working discharges ($B_T = 2.4$ T, $I_p = 250$–300 kA, $n_e = (2$–3$) \times 10^{19}$ m^{-3}, D discharge, duration 1 s); (*b*) smooth structure of the film, deposited in cleaning discharges (inductive 50 Hz Taylor-type D discharge, $B_T = 0.02$ T). Atomic force microscope data.

after opening could detect any Li traces at the side opposite to Li getter. This phenomenon is definitely connected with the high efficiency of the Li screening by the limiters. A quantitative analysis of the Li distribution over the surface of the rail limiter after opening was carried out. As Li after two weeks of exposure to atmosphere converts to the final white dust of Li_2CO_3, its distribution was estimated by the degree of local 'whiteness'. The evidence of high screening by the circular limiter is the rapid decay of the density of Li dust in the shadow of the circular limiter with a characteristic decay length of 11 mm. It corresponds to a decrease in the Li density by a factor of 100 at the wall in the 50 mm limiter shadow.

The absolute Li outflux was estimated by means of the injection of Li pellets by a pneumatic gun. As the large lithium pellet burns out deeply in the plasma column (2/3a), the edge screening of the limiters did not prevent Li from spreading over the whole plasma. In addition, the MHD reconnection process induced by a large pellet also facilitates Li penetration to the plasma centre. Thus, we can consider that the fast increase in particle number in the plasma is due to Li injection. The increase in the plasma density and the decay rate was controlled by an 8-channel interferometer. It was possible to calculate the Li outflux from the plasma by assuming that all density increase and the density decay were due to Li. Experiments showed that under stationary conditions the Li influx was significant only near the limiter (where the evaporation was performed), so the brightness of the Li lines away from the limiter should be determined only by recombination of the Li outflux. Thus the relative increase in Li lines gives information about the stationary Li outflux. The Li outflux was calculated from the decay rate of the total number of particles after injection. The integral outflux of Li ions was 2×10^{20} ions s^{-1}. This value was approximately 10% of the integral deuterium influx. Assuming equal penetration probability of Li and D to the core, we can estimate Z_{eff} of about 1.6. As the experimentally measured value $Z_{eff} = 1.1$–1.2, the penetration probability of Li should be lower than that of deuterium by a factor of 3–6. In fact, Li penetration probability must be much lower, as carbon and iron still should be the main contributors to Z_{eff} [20].

8. Experiments with film deposition

The sputtering of limiters and co-deposition of carbon and tritium are the important issues for a tokamak reactor. The redeposition of carbon, sputtered from the graphite limiters, was investigated in T-10 by exposure of the mirrors and samples at different points of the SOL. Redeposition was investigated separately in working as well as cleaning discharges. Note that for working discharges the probes were at room temperature, and the exposure process in stable working discharges was influenced by the typically unstable current ramp/down phases. Composition of the films was measured using electron probe microanalysis (EPMA). Surface structure and morphology were investigated by optical and electron microscopes and by a profilometer. The thickness and optical parameters (refractive index and extinction coefficient) of the films were estimated by ellipsometry. For the working discharges ($B_T = 2.4$ T, $I_p = 250$–300 kA, $n_e = (2$–3$) \times 10^{19}$ m^{-3}, deuterium discharge, duration—1 s) the deposition rate was 0.08 nm s^{-1} at a position far (about 2.5 m) from the graphite limiters. However, in the close vicinity to the limiter it increased up to 0.5 nm s^{-1}, i.e. more than an order of magnitude. The deposited films were amorphous and consisted of carbon and deuterium (with a typical ratio 3/2–2/1) without any metallic species. In the cleaning discharge (inductive 50 Hz Taylor-type discharge in D, $B_T = 0.02$ T) the deposition rate was 0.008 nm s^{-1}, that is more than an order lower than that for the working one. However, due to the long duration it substantially contributes to the total redeposition of the sputtered carbon. The films' surface was observed with an atomic force microscope. The results in working and cleaning discharges are presented in figures 14(*a*) and (*b*), respectively. The significant difference of the films' surfaces in two cases is clearly seen. In working discharges the deposited films have the feature of a globular structure, while such a feature is practically absent for the cleaning discharges.
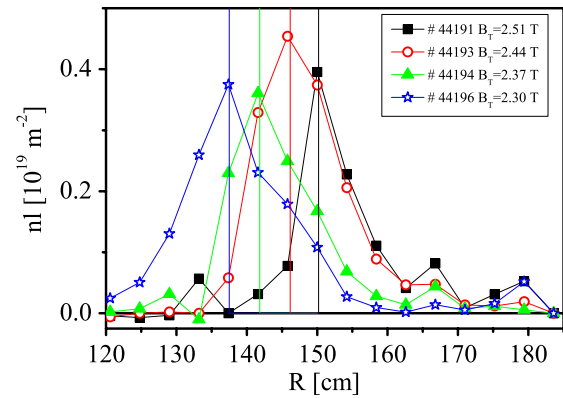
Figure 15. Time evolution of the plasma parameters during density limit disruption in (*a*) ohmic plasma and (*b*) during ECRH heating ($P_{EC\_abs} \sim 1$ MW). Here, P_{bol}—total radiated power, dB_p—poloidal magnetic field perturbations, I_{HR}—hard x-ray and neutron radiation, n_e—plasma density, I_p—plasma current, P_{EC}—ECRH power, I_{D_α}—intensity of the D_α emission. The bursting MHD modes and the radiation bursts (see P_{bol}) connected with the non-thermal electrons are eliminated during the whole duration of the ECRH pulse.

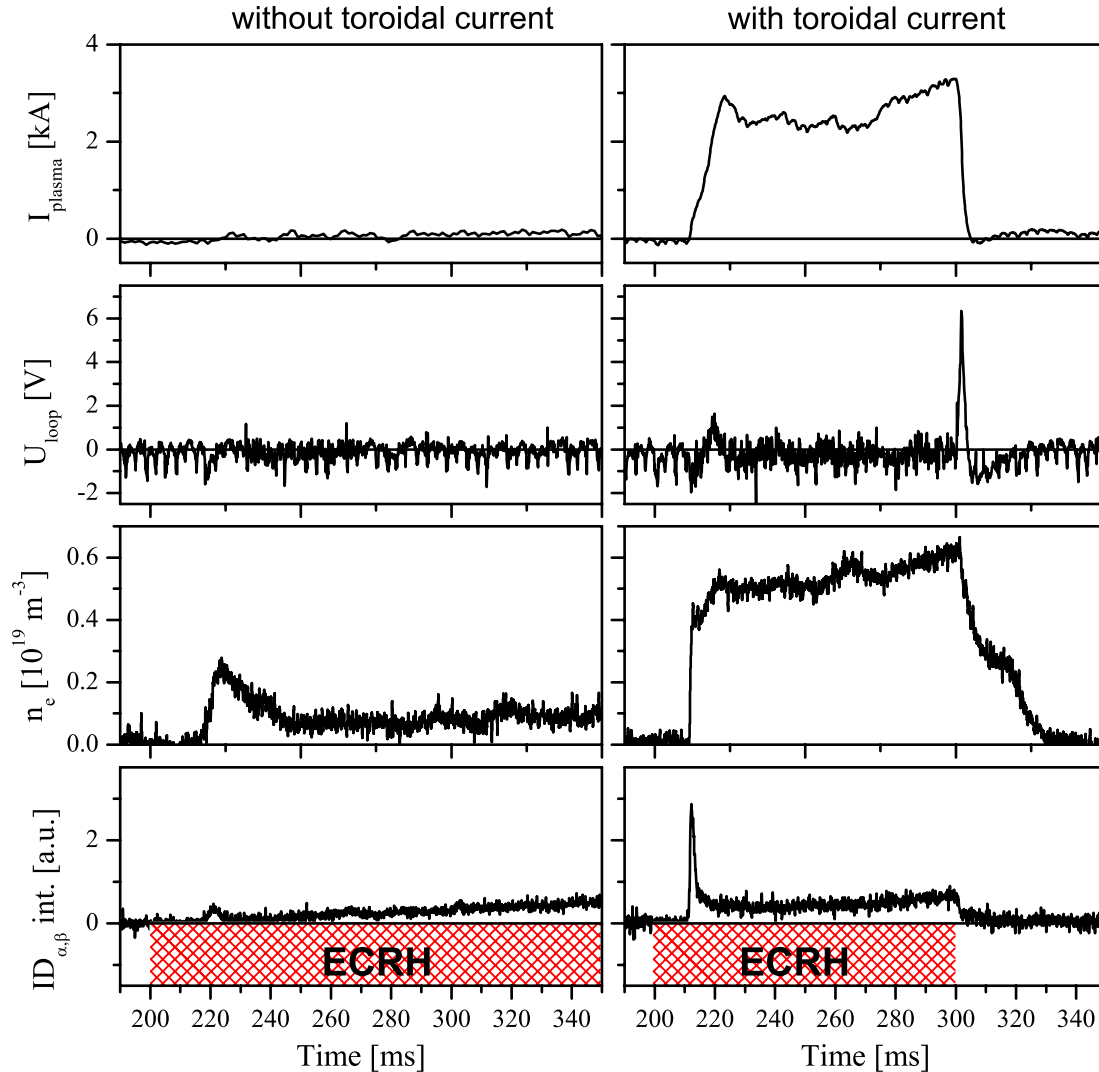## 9. Investigation on runaway electrons control

Bursts of the non-thermal x-ray intensity ($E_\gamma > 100$ keV) are observed in the T-10 plasma during the current decay stage of the density limit disruption. An analysis indicated that the bursts can be connected with non-thermal electrons generated in the plasma core during the magnetic reconnection in a series of minor disruptions. Numerical modelling shows that such periodic generation of the non-thermal electrons can facilitate the production of runaway beams. Application of ECR heating in combination with pre-programmed ohmic power supply system and fast gas puffing allows us to delay, and in some cases to prevent the generation of primarily non-thermal electrons and restoration of the 'quasi-stable' discharge. Numerical modelling indicated that this effect can be connected with modification of the 'equilibrium' current density and pressure profiles with subsequent control of growth rate and amplitude of MHD modes. Time evolution of the non-thermal electrons generated by the electric field is determined in the modelling by balance of the primary Dreicer acceleration and secondary knock-on avalanche, and losses of the non-thermal electrons due to macroscale magnetic turbulence. The magnetic losses depend on the amplitude of the tearing modes (B_r) determined from the analysis of the marginally stable ideal MHD equilibrium subject of the current density profile. Longitudinal electric field is represented by the sum of 'equilibrium' field $E_0(T_e/T_{e0})^{-3/2}$ and electric field induced during the growth of the tearing mode $R/2$ dB_r/dt. Time evolution of the electron temperature T_e is determined using the simplified energy balance equation with the effect of ECRH and periodic enhancement of the electron heat diffusivity proportional to the amplitude of the tearing mode.

Typical evolution of the plasma parameters in experiment with density limit disruptions in OH plasma ($I_p = 0.14$ MA, $B_T = 2.4$ T) is shown in figure 15(*a*) [21]. An additional gas puffing at $t = 600$ ms leads to an increase in the radiation power and growth of the MHD perturbations (dominant harmonic $m/n = 2/1$). The process is terminated

Figure 16. Profiles of chord-integrated electron density in the EC-assisted discharges with different toroidal magnetic fields. Vertical lines show the cold resonance positions.

by the first energy quench ($t = 670$ ms) with subsequent generation of intensive 'bursts' of the bolometric radiation and $D\alpha$ emission ($t = 670$–890 ms). The process is accompanied by decay of the electron density and decrease in the plasma current ($t = 670$–970 ms) and termination of the discharge by switch-off of the T-10 power supply system ($t > 970$ ms). An analysis of the non-thermal x-ray radiation in similar plasma experiments indicated that the 'bursts' are connected with the non-thermal electrons generated periodically during magnetic reconnection in series of minor disruptions. The rate of plasma current decay correlates with the repetition rate of the bursts, which indicates indirectly that current collapse in the T-10 plasma is determined by the step-like process associated with the 'reconnection events' inside the plasma core. Auxiliary plasma heating using EC waves leads to the elimination of radiation bursts and the formation of saturated MHD modes with 'quasi-stationary' amplitude. Typical time evolution of the plasma parameters for this case is shown in figure 15(*b*). Radiation due to the non-thermal electrons is removed for the whole duration of the ECRH pulse and the plasma current
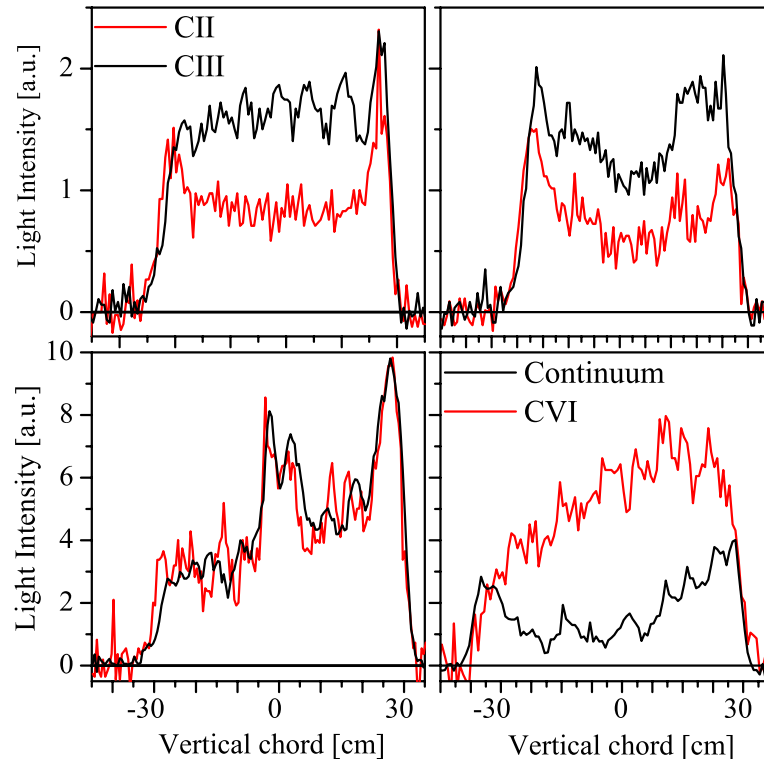
Figure 17. Time traces of main plasma parameters in EC-assisted start-up discharges. Left ones—without toroidal current; right ones—with toroidal current. Parameters (from top to bottom): toroidal plasma current, loop voltage, line-averaged electron density, D_α line intensity.

is sustained. The effect of elimination of the bursting MHD modes and restoration of the hot plasma discharge is observed at relatively high ECRH power ($P_{EC} > P_{OH}$). The threshold power required for the discharge restoration is minimal with the position of the ECRH zone close to the $q = 2$ surface. The threshold power is decreased in discharges with a low plasma current.

10. ECR-assisted breakthrough experiments

The problem of pre-ionization and ECR-assisted start-up is widely discussed now due to the importance of the initial stage of discharge in ITER. It is known that ITER construction leads to restriction of the toroidal electric field at a level of about $0.3\,V\,m^{-1}$, so pure ohmic breakthrough becomes impossible or exists only in a very narrow interval of initial parameters. Previous T-10 experiments demonstrated significant decrease in loop voltage, when power at the second ECR harmonic is applied to the working gas before the start of discharge. Recent experiments were pointed on the physical mechanism of microwave induced pre-ionization and achievement of best

plasma parameters. ECR-only heated plasma was investigated to reveal the nature of the observed effect and exclude the influence of loop voltage. The experimental parameters were $B_T = 2.0$–$2.6\,T$, the initial pressure of working gas $p_0 = (4.5$–$6) \times 10^{-3}\,Pa$, total $P_{EC} \leqslant 0.95\,MW$ at $140\,GHz$. In a special experiment we define the position, where the plasma column begins to form. A 16-channel interferometer was used to observe the radial profile of plasma electron density. The resulted spatial distribution of chord-integral density is shown in figure 16. It is clearly seen that the plasma initiates at the position of cold cyclotron resonance. After breakthrough with $P_{EC} = 0.45\,MW$ and application of vertical magnetic field $B_\perp$, two regimes were observed. The first one is characterized by the absence of the toroidal current I_p, the second one has $I_p = 3$–$8\,kA$ (figure 17). Discharges with non-inductive I_p were achieved with estimated $B_\perp = (1$–$2) \times 10^{-3}\,T$. The nature of this current is the equilibrium currents flowing along the plasma which shorten through the vacuum vessel. It was found that regimes without I_p had narrow electron density and visible lines' intensity profiles (figure 18, left column) with maxima at the ECR position. Discharges with equilibrium current

Figure 18. Comparison of emission profiles for C II and C III lines (top); C VI and recombination continuum (bottom). Left curves correspond to the case without non-inductive toroidal current; right one to the case with toroidal current.

had rather wide profiles, higher visible light emission and significant burn-through of highly ionized carbon ions in the plasma core (figure 18, right column). The temperature T_e was estimated in both types of discharges using the coronal model of light emission by carbon ions. It was found that in discharges without toroidal current $T_e = 5$–10 eV, whereas in the best discharges with current $T_e \leqslant 150$ eV and $n_e = 0.5 \times 10^{19}$ m^{-3}. Thus the discharges with equilibrium current formation are considered as the best candidate for further current rump-up.

11. Future plans

Modernization of the T-10 ECH system is planned: the total heating power will be increased up to $P_{EC} = 4.5$ MW, steering mirrors for ECCD will be available for $P_{EC} = 3$ MW at 140 GHz. Experimental studies in various research areas are under consideration, with special attention to the following

- Further investigation of plasma confinement properties in relation to turbulence characteristics in a wide range of T_e/T_i ratio.
- Studies of disruption physics and mitigation techniques, control tools for MHD stabilization, ECRH assisted start-up.
- Studies of plasma–wall interactions (wall conditioning techniques, formation of carbon films and dust, etc).

Acknowledgments

References

[1] Vershkov V.A. *et al* 2005 *Nucl. Fusion* **45** S203–6
[2] Shelukhin D.A. *et al* 2008 *Proc. 22nd Int. Conf. on Fusion Energy 2008 (Geneva, Switzerland, 2008)* (Vienna: IAEA) CD-ROM file EX/P5-37 and http://www-naweb.iaea.org/napc/physics/FEC/FEC2008/html/index.htm
[3] Waltz R.E., Kerbel G.D. and Milovich J. 1994 *Phys. Plasmas* **1** 2229–44
[4] Gusakov E.Z. and Yakovlev B.O. 2002 *Plasma Phys. Control. Fusion* **44** 2525–37
[5] Tuccillo A. *et al* 2001 *Proc. 28th EPS Conf. on Controlled Fusion and Plasma Physics (Madeira, Portugal, 2001)* vol 25A (ECA) p 65 http://epsppd.epfl.ch/Madeira/html/authors/nav/AutT03fr.html
[6] Timchenko N. *et al* 2009 *Proc. 36th EPS Conf. on Plasma Physics (Sofia, Bulgaria, 29 June–3 July 2009)* vol 33E (ECA) P-5.196 http://epsppd.epfl.ch/Sofia/pdf/P5_196.pdf
[7] Artsimovich L.A. 1972 *Nucl. Fusion* **12** 215
[8] Melnikov A.V. *et al* 2010 *Proc. 37th EPS Conf. on Plasma Physics (Dublin, Ireland, 2010)* vol 34A (ECA) P1.056 http://ocs.ciemat.es/EPS2010PAP/pdf/P1.056.pdf
[9] Melnikov A.V. *et al* 2010 *Proc. 37th EPS Conf. on Plasma Physics (Dublin, Ireland, 2010)* vol O5.128 http://ocs.ciemat.es/EPS2010PAP/pdf/O5.128.pdf
[10] Bugarya V.I. *et al* 1985 *Nucl. Fusion* **25** 1701
[11] Melnikov A.V. *et al* 2007 *Fusion Sci. Technol.* **51** 31
[12] Beklemishev A.D. and Horton W. 1992 *Phys. Fluids* B **4** 200
[13] Waltz R.E. *et al* 2006 *Phys. Plasmas* **13** 052301
[14] Kadomtsev B.B. 1992 *Plasma Phys. Control. Fusion* **34** 1931

[15] Kishimoto Y. *et al* 2000 *Nucl. Fusion* **40** 667
[16] Razumova K.A. *et al* 2006 *Plasma Phys. Control. Fusion* **48** 1373
[17] Joffrin E. *et al* 2003 *Nucl. Fusion* **43** 1167
[18] Andreev V.F. *et al* 2010 *Proc. 23rd Int. Conf. on Fusion Energy (Daejeon, South Korea, 2010)* (Vienna: IAEA) CD-ROM file EXC/P4-01 and http://www-naweb.iaea.org/napc/physics/FEC/FEC2010/html/index.htm
[19] Neudatchin S.V. *et al* 2010 *Proc. 23rd Int. Conf. on Fusion Energy 2010 (Daejeon, South Korea 2010)* (Vienna: IAEA)

CD-ROM file EXC/P4-09 and http://www-naweb.iaea.org/napc/physics/FEC/FEC2010/html/index.htm
[20] Vershkov V.A. *et al* 2008 *Proc. 22nd Int. Conf. on Fusion Energy (Geneva, Switzerland, 2008)* (Vienna: IAEA) CD-ROM file EX/P4-14 and http://www-naweb.iaea.org/napc/physics/FEC/FEC2008/html/index.htm
[21] Savrukhin P.V. *et al* 2010 *Proc. 23rd Int. Conf. on Fusion Energy (Daejeon, South Korea, 2010)* (Vienna: IAEA) CD-ROM file EXW/10-2Ra and http://www-naweb.iaea.org/napc/physics/FEC/FEC2010/html/index.htm